The mechanical response of a magma chamber with poroviscoelastic crystal mush

Yang Liao[1], S. Adam Soule[1], Meghan Jones[1,2], Hélène Le Mével[3]

[1]Woods Hole Oceanographic Institution, Woods Hole, MA, USA
[2]Massachusetts Institute of Technology, Cambridge, MA, USA
[3]Department of Terrestrial Magnetism, Carnegie Institution for Science, Washington, DC, USA

Key Points:

- Features of magma chamber deformation with poroviscoealstic crystal mush are examined using a mechanical model
- Coexistence of poroelastic diffusion and viscoelastic relaxation causes non-monotonous evolution in pressure, stress, and magma transport, after a magma injection event
- The evolution of magma chamber is described by two characteristic time scales depending on the material properties

Corresponding author: Yang Liao, yliao@whoi.edu

Abstract

Improved understanding of the impact of crystal mush rheology on the response of magma chambers to magmatic events is critical for better understanding crustal igneous systems with abundant crystals. In this study, we extend an earlier model by (Liao et al., 2018) which considers the mechanical response of a magma chamber with poroelastic crystal mush, by including poroviscoelastic rheology of crystal mush. We find that the coexistence of the two mechanisms of poroelastic diffusion and viscoelastic relaxation causes the magma chamber to react to a magma injection event with more complex time-dependent behaviors. Specifically, we find that the system's short-term evolution is dominated by the poroelastic diffusion process, while its long-term evolution is dominated by the viscoelastic relaxation process. We identify two post-injection timescales that represent these two stages and examine their relation to the material properties of the system. We find that better constraints on the poroelastic diffusion time are more important for the potential interpretation of surface deformation using the model. We also find that the combination of the two mechanisms causes magma transport to reverse direction in the system, which would successively expose crystals to magma with different chemical compositions.

1 Background: magma chamber model with poroelastic/viscoelastic mush

Petrological studies and thermodynamic models have long indicated that crustal magmatic reservoirs (i.e., magma chambers) contain an abundance of crystal mush, where 'mush' refers to a system with melt contained in a framework of crystals (Cashman et al., 2017). In recent decades, many research efforts have been devoted to understanding how crystal mush evolves and interacts with magma, using principles in thermodynamics, geochemistry, and geophysics. These models demonstrate the importance of crystal mush in a magma chamber's thermal and chemical evolution, as well as in some physical processes such as the segregation of a liquid phase (Sparks & Cashman, 2017; Bachmann & Huber, 2016; Singer et al., 2018; McKenzie, 2011, e.g.,). However, fewer studies have evaluated the impact of crystal mush on magma chamber deformation, pressurization, stress evolution in the host rocks and surface deformation (Gudmundsson, 2012; Liao et al., 2018). Liao et al. (2018) demonstrated that crystal mush can significantly alter the response of a mushy chamber to magma injection events relative to the conventional mush-less, fluid-filled chamber. The model examined two possible rheologies of crystal mush, poroelasticity and viscoelasticity, which are two end members of a more general rheology of poroviscoelasticity. Liao et al. (2018) showed that poroelasticity and viscoelasticity cause similar features in the magma chamber's post-injection evolution (e.g., post-injection pressure decrease and stress increase), but did not examine how the chamber behaves when poroelastic and viscoelastic mechanisms coexist. Here, we expand on the poroelastic/viscoelastic model in (Liao et al., 2018) to explore the effects of poroviscoelastic mush on the response of a magma chamber to a magma injection event and the resulting ground deformation.

2 Magma chamber model with poroviscoelastic mush in a half-space

For ease of comparison with previous mechanical magma chamber studies (Dragoni & Magnanensi, 1989; Karlstrom et al., 2010; McTigue, 1987; Segall, 2016; Liao et al., 2018, e.g.,), we adopt the same spherical geometry of the poroelastic chamber model as (Liao et al., 2018) shown in Figure 1a. The magma chamber consists of a spherical core of liquid magma within a shell of poroviscoelastic mush with pre-injection porosity ϕ_o. The magma chamber is hosted in a half space of linear elastic crust with a traction-free upper surface. We approximate the surface deformation in vertical and horizontal direc-

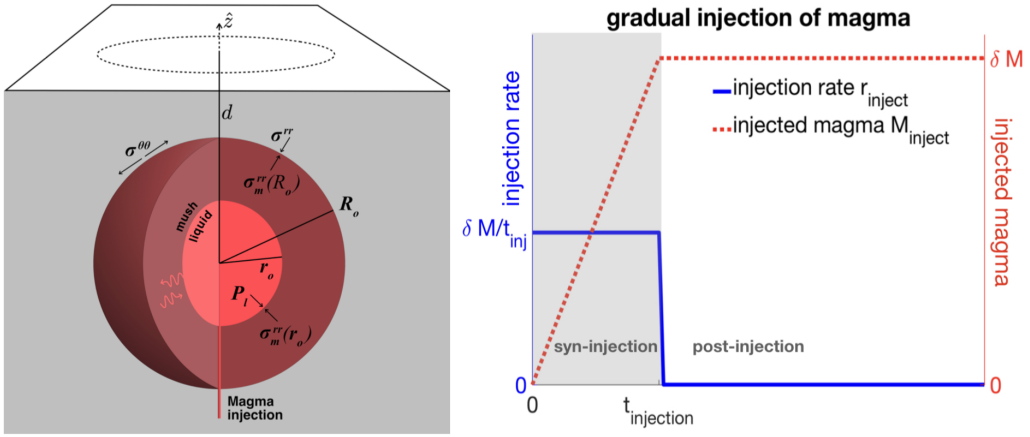

[H]

Figure 1. (a) geometry of the mushy magma chamber model (adapted from (Liao et al., 2018)), with several important quantities marked including: core pressure P_l, pore pressure P_f, tensile stress $\sigma^{\theta\theta}$, force balance on the two interfaces, and transport of magma in the mush region (red curved arrows). The chamber is at depth d from a free surface with radius R_o and liquid core radius r_o. (b) accumulated amount of injected magma M_{inject} (y axis on the right) and injection rate r_{inject} (y axis on the left) as functions of time, t_{inj} is the length of the injection. The shaded area indicates the syn-injection period $0 \leq t \leq t_{inj}$.

tions following the same approach used in earlier studies (Segall, 2016, 2019; McTigue, 1987).

We assume a simplified magma injection event, where magma enters into the liquid core at a constant injection rate during the injection period $0 \leq t \leq t_{inj}$ (Figure 1b), leading to the accumulated mass of injected magma $M_{inject} = \frac{t\delta M}{t_{inj}}$ for $t \leq t_{inj}$ and $M_{inject} = \delta M$ for $t > t_{inj}$.

During and after the injection, magma is allowed to flow across the liquid-mush interface and within the mush, driven by the gradient of pore pressure P_f. The motion of pore magma follows Darcy's law and mass conservation

$$\vec{q} = -\frac{\kappa}{\eta_f}\nabla P_f \tag{1a}$$

$$\frac{\partial m}{\partial t} + \nabla \cdot (\rho_f \vec{q}) = 0 \tag{1b}$$

where $\vec{q}$ is the Darcy velocity (positive values indicates the flow direction from magma core to the chamber wall), κ is the permeability of the mush, η_f is the magma viscosity, and ρ_f is the density of pore magma. The variation in fluid content is described by the function $m(r,t)$, which is defined as the change in pore fluid mass per un-deformed volume of mush located at radius r (positive value $m > 0$ indicates that the pores in the mush gain magma). The integration of m across the mush shell leads to the total amount of magma transported between the liquid and the mushy region

$$M_{leak} = \int_{r_o}^{R_o} 4\pi r^2 m(r,t) \mathrm{d}r \tag{2}$$

where $M_{leak}(t)$ is the accumulated amount of magma transported across the magma-mush boundary. $M_{leak} > 0$ indicates that magma is flowing from the liquid core to the mushy shell (i.e., 'leaking'). We calculate the pressure change P_l in the liquid core upon mass injection assuming isothermal compression, which depends on the amount of injected magma M_{inject}, the amount of magma exchanged between the core and mush M_{leak}, and the volume change of the liquid core indicated by the radial displacement $u_m(r_o)$ on the core-mush interface. After linearization, the pressure change is (Liao et al., 2018):

$$P_l(t) = K_l(\frac{M_{inj}(t)}{M_o} - \frac{M_{leak}(t)}{M_o}) \left(1 - 3\frac{u_m(r_o,t)}{r_o}\right) \tag{3}$$

where K_l is the bulk modulus (1/compressibility) of the core and injected magma, and M_o is the pre-injection magma mass in the liquid core (see Appendix Appendix A). The injection causes the chamber to inflate, which leads to increased displacement $\vec{u}_{rock}$ and elastic stress $\boldsymbol{\sigma}_{rock}$ in the surrounding crustal rocks, following the constitutive relation for linear elastic material

$$\boldsymbol{\sigma_{rock}} = (K_r - \frac{2}{3}\mu_r)\nabla \cdot \vec{u}_{rock}\boldsymbol{I} + \mu_r \left(\nabla\vec{u}_{rock} + \nabla\vec{u}_{rock}^T\right) \tag{4}$$

where K_r and μ_r are the bulk and shear modulus of the host rock, respectively. It is worth noting that the stress component in the tensile direction $\sigma^{\theta\theta}$ on the chamber-rock boundary (Figure 1a) increases during the inflation of the chamber, which, when exceeding the tensile strength of the host rock, may cause the chamber's wall to rupture (Grosfils, 2007; Zhan & Gregg, 2019; Currenti & Williams, 2014; Karlstrom et al., 2010; Gudmundsson, 2012, e.g.,) (a process we omit in the current model). We describe the deformation and stress in the crystal mush using a poroviscoelastic rheology, combining linear poroelasticity with a Maxwell viscoelastic model. The strain $\boldsymbol{\epsilon}_m$, stress $\boldsymbol{\sigma}_m$, variation in fluid content m and pore pressure P_f obey the constitutive relations

$$\left(\frac{\partial\boldsymbol{\sigma}_m}{\partial t} + \frac{\mu_m}{\eta_m}\boldsymbol{\sigma}_m\right) - \frac{1}{3}\frac{\mu_m}{\eta_m}Tr(\boldsymbol{\sigma}_m)\mathrm{I} = 2\mu_m\frac{\partial\boldsymbol{\epsilon}_m}{\partial t} + \left(K_m - \frac{2}{3}\mu_m\right)\frac{\partial Tr(\boldsymbol{\epsilon}_m)}{\partial t}\mathrm{I} - \alpha\frac{\partial P_f}{\partial t}\mathrm{I} \tag{5a}$$

$$m = \rho_f\alpha\left(Tr(\boldsymbol{\epsilon}_m) + \frac{\alpha}{K_u - K_m}P_f\right) \tag{5b}$$

where K_m is the bulk modulus of the crystalline framework (i.e., drained modulus), and K_u is the bulk modulus of the crystal-fluid ensemble (i.e., undrained modulus). α is the poroelastic constant (also known as Biot constant) with a value from 0 to 1, determined by the strength of the crystalline framework relative to that of the single crystal (represented by its bulk modulus K_s) as $\alpha = 1 - \frac{K_m}{K_s}$. We assume that the crystalline network itself is weak compared to the single crystals, thus $K_m << K_s$, leading to a large α. We use $\alpha = 0.9$ for the rest of the study. The viscoelastic relaxation of the crystalline matrix is determined by its rigidity μ_m and viscosity η_m. We can verify that the poroelastic and viscoelastic rheologies are two end members of the poroviscoelastic rheology: when matrix viscosity $\eta_m \to \infty$, (5) reduces to linear poroelasticity (Cheng, 2016); when pore pressure is decoupled from the stress (i.e., $\alpha = 0$), (5) becomes the classical Maxwell formulation (Segall, 2016; Jellinek & DePaolo, 2003).

The deformation in the host rocks and the mush shell obey quasi-equilibrium condition

$$\nabla \cdot \boldsymbol{\sigma}_{m,rock} = 0 \tag{6}$$

and boundary conditions,

$$P_l + \sigma_m^{rr}(r_o) = 0 \tag{7a}$$
$$P_l - P_f(r_o) = 0 \tag{7b}$$
$$\sigma_m^{rr}(R_o) - \sigma_{rock}^{rr}(R_o) = 0 \tag{7c}$$
$$\vec{u}_m(R_o) - \vec{u}_{rock}(R_o) = 0 \tag{7d}$$
$$\frac{\partial P_f}{\partial r}(R_o) \tag{7e}$$
$$u_{rock}(r \to \infty) = 0 \tag{7f}$$

which prescribes force balance, continuity (in displacement and fluid pressure) at both the magma-mush and mush-rock boundaries, and a chamber wall impermeable to the pore magma. The above constraints determine the unique time-dependent solutions, which are calculated using Laplace transform (see Appendix Appendix A). We follow earlier studies to approximate the surface deformation resulting from the deformation of a spherical chamber (McTigue, 1987; Segall, 2016, 2019)

$$\begin{aligned} u_z(\rho,t) &= -\frac{\sigma_m^{rr}(R_0,t)}{\mu_r}\frac{R_0^3}{d^2}\frac{1-\nu}{\left(\frac{\rho^2}{d^2}+1\right)^{\frac{3}{2}}} \\ u_\rho(\rho,t) &= -\frac{\sigma_m^{rr}(R_0,t)}{\mu_r}\frac{R_0^3}{d^2}\frac{1-\nu}{\left(\frac{\rho^2}{d^2}+1\right)^{\frac{3}{2}}}\frac{\rho}{d} \end{aligned} \tag{8}$$

where u_z and u_ρ are the vertical and horizontal displacement on the surface $z = 0$, measured at a radial distance ρ; ν is the Poisson's ratio of the elastic crust, σ_m^{rr} is the radial component of stress at the chamber-crust interface. Earlier works demonstrated that when the depth of the magma chamber d is modestly larger than the chamber's radius $d/R_0 \geq 2$, (8) provides good estimations for the deformation on the surface (Segall, 2016). In our study, we assume d/R_0 between 3 to 10 for precise approximation of the ground deformation. Because the poroviscoelastic mush is subjected to two different mechanisms (poroelastic diffusion and viscoelastic relaxation), we identify two timescales that represent the two mechanisms respectively (see Appendix Appendix A)

$$\tau_{diffusion} = \frac{R_o^2\eta_f}{\kappa}\frac{\alpha^2\left(K_u+\frac{4}{3}\mu_m\right)}{(K_u-K_m)\left(K_m+\frac{4}{3}\mu_m\right)} \tag{9a}$$
$$\tau_{relaxation} = \frac{\eta_m}{\mu_m} \tag{9b}$$

where $\tau_{diffusion}$ is the poroelastic diffusion time and $\tau_{relaxation}$ is the viscoelastic relaxation time. We verify that the crystal mush is poroelastic when $\tau_{relaxation} = \infty$, and viscoelastic if $\tau_{diffusion} = \infty$. Given the uncertainties in parameters such as mush permeability, crystalline rigidity and viscosity, magma viscosity and compressibility, $\tau_{relaxation}$ and $\tau_{diffusion}$ can have a wide range of values. For example, the poroelastic diffusion time $\tau_{diffusion}$ ranges from 6 days to 160 years assuming a magma chamber with 1km radius and parameters similar to those used in (Liao et al., 2018) and others ($\alpha = 0.9$, $\mu_m^o = 1$ GPa, $K_f = 1$ GPa, $\kappa \in [10^{-10}, 10^{-8}]m^2$, and $\eta_f \in [10^1, 10^3]$ Pa.s). Further, assuming a crystalline viscosity similar or smaller than heated rock ($\eta_m \in [10^{16}, 10^{18}]$ Pa.s), the resulting viscoelastic relaxation time $\tau_{diffusion}$ ranges from 4 months to 30 years (Segall, 2016; Cheadle et al., 2004; McKenzie, 2011). Below, we choose the case of a poroviscoelastic mush subjected to both mechanisms with comparable time scales $\tau_{diffusion} = \tau_{relaxation}$ to illustrate the basic features of a poroviscoelastic mushy chamber.

It is worth noting that, although the current model fill in the gap in rheology assumed in (Liao et al., 2018), many assumptions are still made to simplify the problem.

These assumptions, including the spherical geometry, radial symmetry in magma chamber deformation, homogeneity in crystal mush distribution, and neglected thermal effects could all affect how a more realistic mushy magma chamber reacts to magma injection, and, while beyond the scope of this study, should be examined and evaluated in future studies.

3 Model results

Similar to poroelastic or viscoelastic mush, the poroviscoelastic mush causes the magma chamber and its surrounding crust to continue evolving after the injection has stopped, as opposed to a fluid chamber that reaches steady state as soon as the injection ends (Figure 4). We find that the time-dependent evolution of the poroviscoelastic mushy chamber is, at different times, dominated by either poroelastic diffusion or viscoelastic relaxation. Below, we examine the features of deformation, pressure, stress, and magma transport in both stages.

3.1 Syn- and post- injection evolution of magma chamber with poroviscoealstic mush shell

We examine time-dependent magma chamber deformation during three stages: syn-injection, shortly after the injection, and long the after the injection. During the syn-injection period, magma is added into the liquid core at a constant rate (shaded area in Figure 1b), increasing the pressure in the core magma (Figure 4a), and pushing both the magma-mush boundary at $r = r_o$ and the mush-rock boundary at $r = R_o$ outward (Figure 3a). The expansion of the whole chamber causes the tensile stress in the rock surrounding the chamber and ground deformation to increase with time (Figure 4b, c). During the syn-injection period, pressure in the liquid core always exceeds the pore pressure in the mush shell. As a result, some magma in the liquid core flows into the mush (Figure 5a), increasing the pore pressure in the mush (See Figure B2 in Appendix Appendix B). The syn-injection period ends at $t = t_{inj}$, when the injection rate drops to 0. At the end of the injection, a fluid pressure gradient remains that sustains magma flow from the core fluid into the mush.

The short post-injection period begins when the injection stops, at $t = t_{inj}$. During this period, the evolution of the deformation is similar to that of a chamber with poroelastic mush (see Figure 3b in (Liao et al., 2018)). Without more magma injection, the fluid core loses magma due to porous flow into the mush, causing the pressure in the liquid core to decrease. The liquid-mush boundary retracts inward and the liquid core shrinks in response to the decreasing core pressure and mush expansion (Figure 5b, Figure 4a, Figure 3b). Although viscous relaxation also occurs during this period, it is not strong enough to noticeably deviate the evolution of the system from that of a poroelastic chamber. Because of these qualitative similarities, we consider the short time period post-injection evolution to be dominated by the poroelastic diffusion mechanism (middle panel in Figure 2).

With time, the effect of viscoelastic relaxation becomes more apparent – as the poroelastic effects diminish – and the system begins to show features similar to those displayed by a purely viscoelastic mushy chamber. During this period, the viscoelastic relaxation causes outward creeping and compression of the whole mush shell (Figure 3c), reversing the motion of the previously retracting liquid-mush boundary and pushing it outward again (Figure 2b). The outward movement of the liquid-mush boundary causes the volume of the liquid core to expand, and the pressure in it to further decrease (Figure 4a). The outward creeping of the mush-rock boundary causes the tensile stress in the host rock and ground deformation to continue increasing (Figure 4b, Figure 8a). Eventually, the liquid core pressure becomes less than the pore pressure in the adjacent mush due to the loss of core magma and the expansion of the core. This reverses the pressure gra-

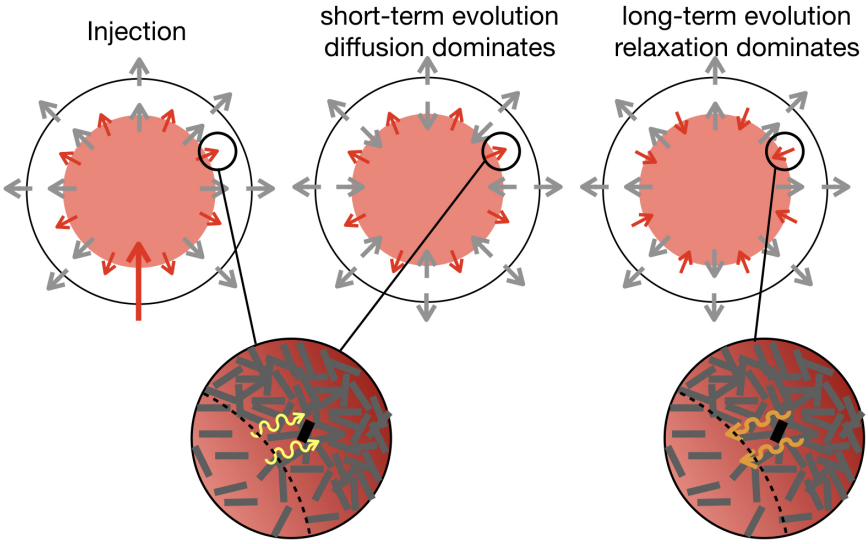

Figure 2. Cartoon illustration of the three stages in the dynamic evolution of a mushy magma chamber: syn-injection stage, poroelastic diffusion-dominated stage, and viscoelastic relaxation-dominated stage. Grey arrows indicate the direction of the radial displacement of the magma-mush and mush-rock boundaries, and red arrows show the direction of magma transport. Illustration of pore magma transport and their possible chemical signatures are shown in the zoom-in panels. The deformation dominated by poroelastic diffusion is consistent with the evolution shown in Figure 3(b), and the viscous relaxation-dominated regime is consistent with Figure 3(c).

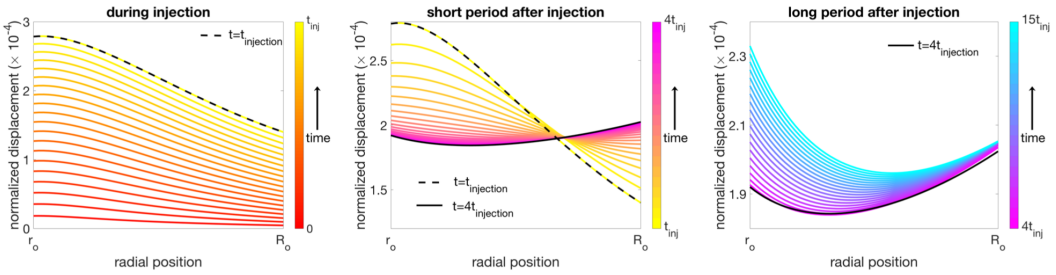

Figure 3. Displacement in the poroviscoelastic mush shell during and after injection. Left panel shows the displacement $u(r)/R_o$ (normalized by the chamber radius) as a function of radial position r during the injection $0 \leq t \leq t_{injection}$, where black dash line indicate the displacement profile at the end of the injection $t = t_{injection}$; middle panel shows the displacement during a short time period after the injection $t_{injection} \leq t \leq 4t_{injection}$, where the black dash line and black solid line show the profile at $t = t_{injection}$ and $t = 4t_{injection}$, respectively; right panel shows the displacement for longer period after the injection $t > 4t_{injection}$, where the black solid line indicates the profile at $t = 4t_{injection}$. The left and middle panels are qualitatively similar to the evolution of a poroelastic shell (see Figure 3 in (Liao et al., 2018)). The poroelastic dominated and viscoelastic dominated deformations are also shown in cartoon illustration in Figure 2.

dient direction at the magma-mush boundary resulting in porous flow from the mush into the core (Figure 5c), returning most of the previously leaked magma back into the core (Figure 6). This stage, where the magma chamber is dominated by viscoelastic relaxation, lasts until the system reaches a new steady state. Although the decrease in chamber pressure and increase in tensile stress of the crust during this period are similar in sign to the poroelastic diffusion dominated stage, the rate of change in these quantities is much lower, as is reflected by a nearly indiscernible strain rate at the wall of the chamber (Figure B1 in Appendix Appendix B) and slow increase in ground elevation (Figure 8).

3.2 Timescales in post-injection evolution

Compared to the poroelastic case where one timescale can be identified to describe its post-injection evolution (Liao et al., 2018), a chamber with poroviscoealstic mush requires two timescales to characterize the non-monotonic changes in pressure, stress, and magma transport (Figure 4 and 6). To determine the short-period evolution time t_{post}^{short}, we numerically calculate the time it takes for the pressure gradient at the magma-mush interface to reverse, and for magma to begin to leak back into the liquid core (Figure 6b) after a sudden injection. To determine the long-period evolution time t_{post}^{long}, we calculate the time it takes for the system to approach a final steady state after injection, using the same analytical approach in (Liao et al., 2018) for a poroelastic/viscoelastic chamber. Following a sudden injection at $t = 0$, the evolution of the system during time period $0 < t \leq t_{post}^{short}$ is consistent with a poroelastic diffusion dominated stage, represented by a relatively rapid decrease in chamber's pressure P_l, a rapid increase in tensile stress $\sigma^{\theta\theta}$, and core-to-mush magma transport. Over the time period $t_{post}^{short} < t \leq t_{post}^{long}$, the system behaves consistently with a viscoelastic relaxation dominated stage, characterized by a slower decrease in chamber's pressure, slow increase in tensile stress, and mush-to-core magma transport. Over the time period $t > t_{post}^{long}$, the system remains dom-

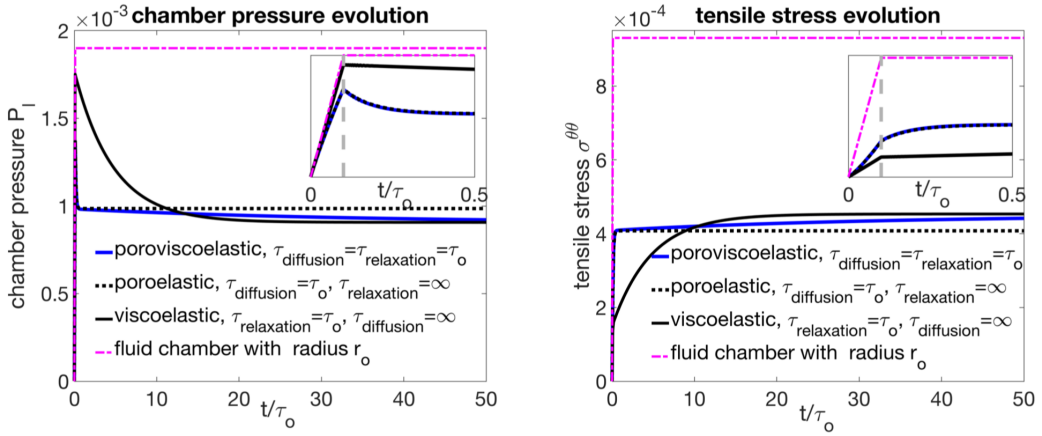

Figure 4. Syn- and post-injection evolution of liquid core fluid pressure P_l (panel a), and tensile stress $\sigma^{\theta\theta}$ (panel b) as functions of time, with initial short period evolutions zoomed in insert panels. Purple broken line corresponds to a mushless liquid chamber with the mushy chamber's liquid core radius $r_0 = 0.5R_0$; blue solid lines, black dotted lines, and black solid lines correspond to a mushy chamber with poroviscoelastic, poroelastic, or viscoelastic mush shell respectively.

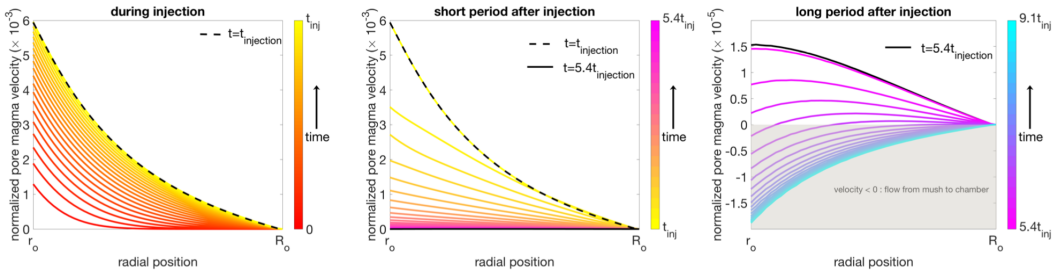

Figure 5. Darcy velocity of pore magma $\vec{q}$ (radial component) in the poroviscoelastic mush shell, as a function of radial position r, during and after injection. The velocity is normalized by velocity scale $\kappa\mu_r/\eta_f R_o$, where κ is the mush permeability, μ_r is the crustal rock rigidity, η_f is the viscosity of pore magma, and R_o the radius of the chamber. Positive values of q indicate the magma flowing from the core to the mush, and negative values indicate flow from the mush into the core. Left panel corresponds to syn-injection evolution $0 \leq t \leq t_{injection}$, where the black dash line indicates the velocity profile at the end of the injection $t = t_{injection}$; middle panel shows the pore magma velocity during a short time period after the injection $t_{injection} \leq t \leq 5.4t_{injection}$, where the black dash line and black solid line show the profile at $t = t_{injection}$ and $t = 5.4t_{injection}$, respectively; right panel shows the velocity for longer period after the injection $t > 5.4t_{injection}$, where the black solid line indicates the profile at $t = 5.4t_{injection}$. The poroelastic dominated and viscoelastic dominated pore magma flow direction are also shown in cartoon illustration in Figure 2. The region where $q < 0$ in the right panel indicates the change in flow direction of the pore magma, which corresponds to the onset of decrease in the amount of cumulated leaked magma (see Figure B2 in Appendix Appendix B).

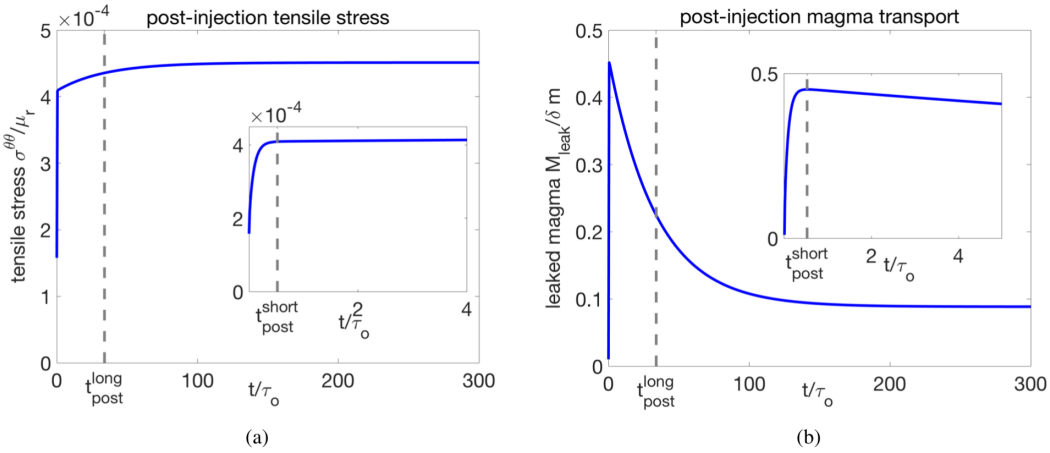

Figure 6. Post-injection short-term (insert panels) and long-term evolution of tensile stress (left) and leaked magma M_{leak} (right) from the liquid core to the shell following a sudden injection. Grey dashed lines indicate the two post-injection timescales t^{long}_{post} and t^{short}_{post} identified for the post-injection evolution.

inated by viscoelastic relaxation, although its evolution is slow enough to be regarded as approaching a new steady state.

We found that both t^{short}_{post} and t^{long}_{post} depend on the material properties (e.g., $\tau_{diffusion}$ and $\tau_{relaxation}$) and geometry of the system (e.g., r_o/R_o). Although $\tau_{diffusion}$ and $\tau_{relaxation}$ both affect t^{short}_{post} and t^{long}_{post}, it is clear that the short-period evolution time t^{short}_{post} is more sensitive to $\tau_{diffusion}$; whereas the long-period evolution time t^{long}_{post} changes more sensitively with $\tau_{relaxation}$(Figure 7). Considering that the early post-injection evolution of the system corresponds to faster change and higher strain-rate, we consider it to be potentially more relevant to geophysical observations (e.g., deformation, seismicity), hence constraining the value of $\tau_{diffusion}$ is important for comparing the model to field data. According to (9a), $\tau_{diffusion}$ is determined by parameters that are not well constrained for magmatic mush, such as mush permeability κ and magma viscosity η_f. Reasonable variations in these parameters can cause $\tau_{diffusion}$ to vary across orders of magnitudes from days to hundreds of years. For these reasons, better constraints on these parameters via petrological observations and thermodynamic models are crucial for evaluating rheological models such as the one proposed here. It is also worth noting that the two post-injection timescales are defined based on the evolution of magma chamber following a sudden injection, and can qualitatively describe the behavior of a mushy chamber when the injection is much shorter than both $\tau_{diffusion}$ or $\tau_{relaxation}$. For very long injection times (i.e., low injection rates), however, the diffusion-dominated stage becomes very short, and the chamber would qualitatively display characteristics of the relaxation-dominated stage soon after the injection (see Figure B3 in Appendix Appendix B).

3.3 Implications on geodetic and petrologic observations

3.3.1 Implication on the interpretation of ground deformation

One consequence of the existence of mush in a magma chamber is prolonged ground deformation after the injection has ceased due to redistribution of pore magma and/or relaxation of the crystalline framework. For example, a 1.5 km magma chamber at 4.5 km depth undergoing a one-year injection with a moderate rate of $1.12m^3/s$ would experience an additional 30mm of ground uplift (1/3 of total uplift), in the period of three

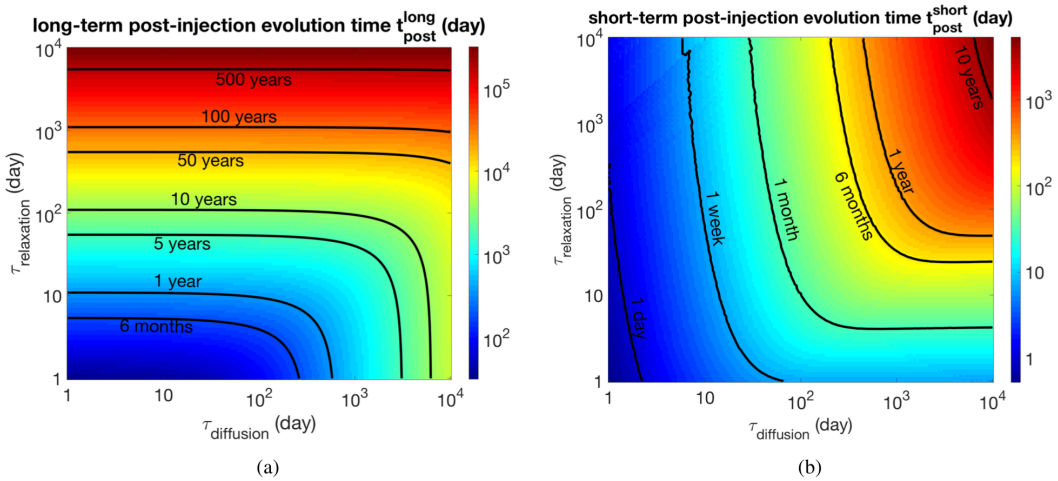

Figure 7. Post-injection short-term evolution timescale t_{post}^{short} (right) and long-term evolution timescale t_{post}^{long} (left) shown as functions of viscoelastic relaxation time $\tau_{relaxation}$ and poroelastic diffusion time $\tau_{diffusion}$. The long-term evolution time t_{post}^{long} is more sensitive to the change in viscoelastic relaxation time; the short-term evolution time is more sensitive to the change in poroelastic diffusion time.

years after the injection has stopped (Figure 8a). For an injection at a constant rate, a mushy chamber results in time-dependent changes in the rate of ground deformation distinct from a liquid chamber hosted in elastic rock. Specifically, our mushy chamber model predicts an increasing syn-injection ground uplift rate, and decreasing post-injection uplift rate, such that the strain rate and uplift rate reach their maximum at the end of the injection (Figure 8b). This characteristics (i.e., increasing then decreasing uplift rates of ground deformation) have been observed at various volcanic systems, for example, at Long Valley Caldera, Campi Flegrei, and Laguna del Maule (Le Mével et al., 2015). At Laguna del Maule volcanic field in Chile, they are explained as consequences of time-varying injection rates (Le Mével et al., 2016). While this is one possible explanation, injection rates in physical models are typically considered to be constant or to decrease exponentially (Segall, 2016; Huppert & Woods, 2002; Biggs & Pritchard, 2017). The mushy chamber model provides an alternative explanation for such features, where the combination of injection, pore magma transport and relaxation modulate deformation rates.

Although the time-dependent features in ground deformation may suggest the existence of a mushy chamber, the magnitude of ground deformation caused by a deforming mushy chamber is limited in its ability to constrain key parameters of the chamber such as its volume, pressure, and likelihood to rupture. Similar to classical models, the depth of the magma chamber d can be straightforwardly obtained from (8) by comparing the vertical and horizontal components of the displacement $d = u_z\rho/u_\rho$ (Segall, 2019). With d and the elastic properties of crustal rock constrained, the ground deformation further constrains $\sigma_m^{rr}V_0 \propto \Delta V$ (or P_lV_0 if there is no mush, ΔV is injected volume), but can not constrain pressure/stress and chamber volume individually. We find that when the depth d is fixed, the amplitude of ground deformation $u_{\rho,z} \propto \Delta V\frac{R_o^3}{r_o^3}$. Therefore the ground deformation increases with the volume ratio of mush and is independent of the size of the chamber (Figure 9): for the same injection event, a large chamber with 50% mush and a small chamber with 50% mush cause the same ground deformation, and that a liquid chamber always causes smaller ground deformation than a mushy chamber, regardless of its size. On the other hand, the pressure and tensile stress depend on both the volume ratio of mush and the total volume of the chamber. Therefore, a small

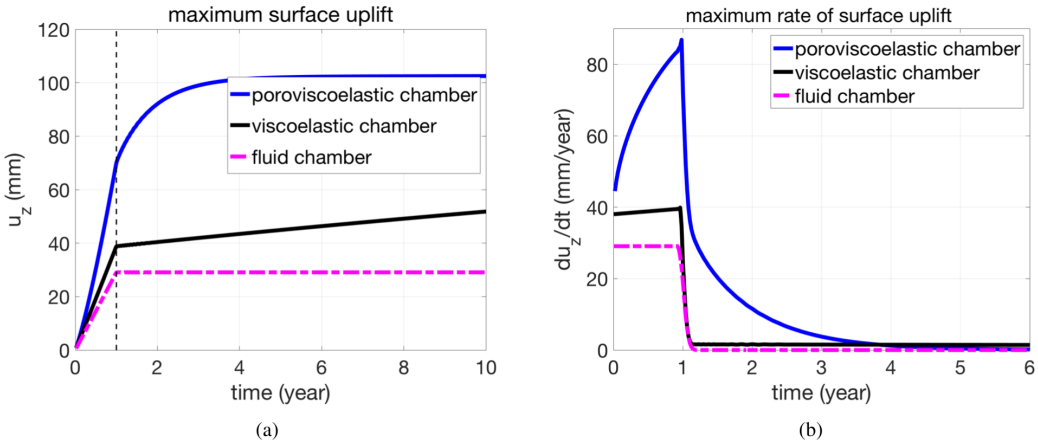

Figure 8. Vertical surface uplift (panel a) and rate of surface uplift (panel b) as functions of time during and after injection, for a liquid chamber (purple broken lines) and a mushy chamber with either poroviscoelastic (blue solid lines) or viscoelastic (black solid lines) mush (diffusion and/or relaxation time $\sim$ 10 years). The center of the magma chamber is located at a depth of 4.5km, with a radius of 1.5km. The injection assumes a volumetric injection rate of $1.12m^3/s$ for the duration of 1 year, indicated by black dash line in panel a. The rate of ground deformation has been smoothed to eliminate numerical artifacts caused by the Laplace inversion algorithm.

liquid chamber may cause smaller ground elevation compared to a large mushy chamber, but is more likely to erupt due to higher pressure and tensile stress. This non-uniqueness poses a challenge to applying our forward models to interpret ground deformation data. Combining ground deformation data with other geophysical measurements, such as seismic and electromagnetic methods, is necessary to provide constraints on the volumes of liquid and mush, and to increase the applicability of models as proposed here (Magee et al., 2018; Ward et al., 2014).

3.3.2 Magma transport and consequence on crystal zoning

The potential for a mushy magma chamber to develop pressure gradients that promote transport into and out of the mush (Figure 2, Figure 6b and Figure B2) offers an additional mechanism to explain observations of zonation in phenocrysts. Chemically zoned phenocrysts are seen as sensitive recorders of magmatic conditions. A variety of processes are linked to zonation including changes in the temperature, composition, pressure, water content, and oxygen fugacity of the host magma (Ruprecht & Wörner, 2007, e.g.,) or by transport of crystals through gradients in physico-chemical properties in a zoned magma chamber (Ginibre et al., 2002, e.g.,). Whereas simple zonation of a mafic core and more evolved rim (or vice versa) are commonly explained by magma mixing events; more complex zonation, including oscillatory zoning, require similarly complex physical mechanisms ((Perugini et al., 2005; Ginibre & Wörner, 2007, e.g.,)). An example from the 2001 eruption of Shiveluch Volcano finds multiple phases with distinct zoning features ((Humphreys et al., 2006)). Sieve textured Ab-rich plagioclase feldspars with overgrowths of An-rich rims are interpreted to reflect the mixing of a hotter, more primitive melt with the existing evolved melt. In the same eruption, oscillatory zoned plagioclase are observed that are interpreted to reflect oscillations in pressure and pH2O resulting from unstable conduit flow during ascent. A subset of oscillatory zoned plagioclase have patchy cores that are typically more anorthitic and are thought to form from a more primitive melt than simple oscillatory zoned phenocrysts.

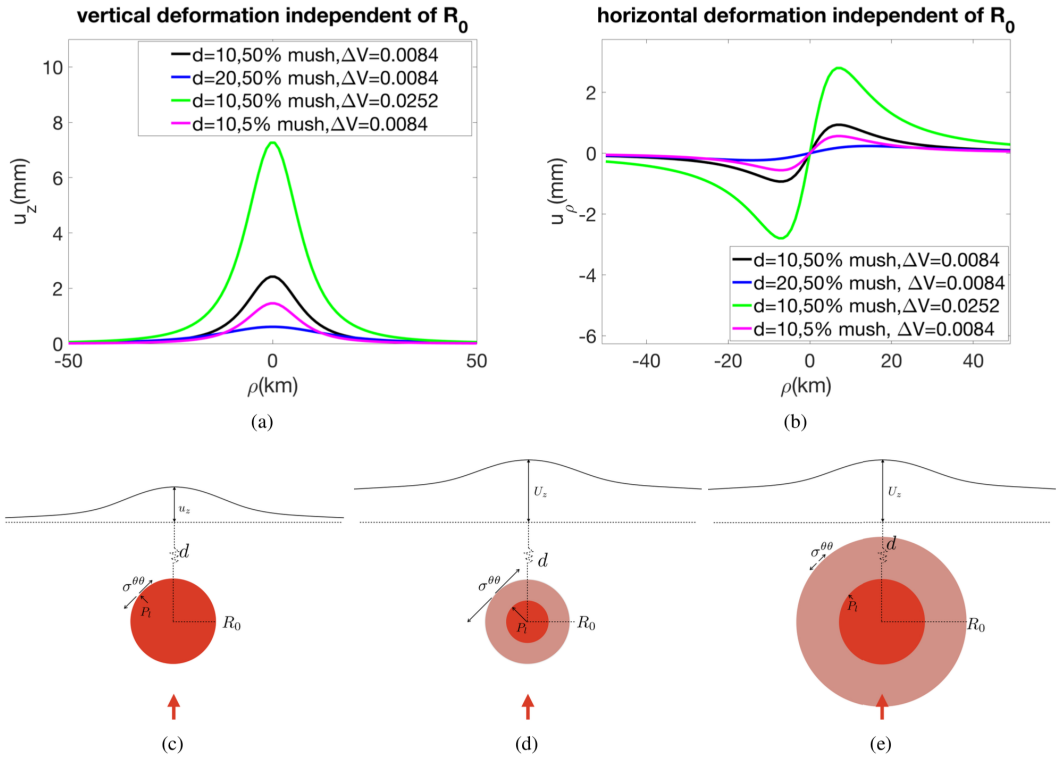

[H]

Figure 9. (a) and (b) show vertical and horizontal displacement at the surface for different combination of burial depth d (km), mush volume fraction, and injected volume ΔV (km^3). The ground deformation increases with mush volume fraction, injected volume ΔV, and decreases with burial depth d, but does not vary with the size of the chamber. (c)-(e) are cartoons illustrating three different magma chambers under the same magma injection. Tensile stress, chamber pressure, and ground deformation in the new steady state ($t \rightarrow \infty$) are shown in all three cases (not to scale). Case (c) represents a liquid chamber with radius r_0; case (d) represents a mushy chamber with total chamber radius r_0; case (e) represents a mushy chamber with liquid core radius r_0. All three chambers are buried at the same depth d and subjected to the same amount of injected magma ΔV. Cases (d) and (e) cause the same ground deformation as they have the same mush volume fraction, but cause different tensile stress and pressure.

These interpretations of distinct mechanisms for zoning are well-supported and another explanation is not necessarily required; however, we postulate that similar zonation features could develop in phenocrysts due to transport of melt in and out of the mush zone. Oscillatory zoning, for example, could form near the melt-mush interface as crystals are washed by outward (e.g., more primitive, hotter) and inward (e.g., less primitive, cooler) melt. Sieve textured phenocrysts might be located further into the mush zone, where only a larger injection event would allow a more primitive melt to encounter the crystals, and which would be less subjected to significant changes in flow direction. In addition to injection-induced pressure gradients, other processes such as vesiculation and or gas loss may also allow melt transport through the mush producing 'in-place'zonation. The potential to produce chemical zonation within magmatic mush merits further examination including the physical processes of disaggregating the mush and the probability of incorporating those crystals into the melt (Parmigiani et al., 2014, e.g.,), and the examination of asymmetric zonation patterns (e.g., non-concentric) that might result in a partially interconnected network of crystals.

4 Summary and discussion

In this study, we extend a previous mechanical model by Liao et al. (2018) on mushy magma chambers with poroelastic or viscoelastic mush, by incorporating a more general mush rheology of poroviscoelasticity. We subject the new mushy magma chamber model to an external perturbation of a magma injection with constant injection rate for a duration of time, and observe the similarities and differences caused by different mush rheology on evolution of pressure, stress, magma transport, and surface elevation. We found that the poroviscoelastic mush display both mechanisms of poroviscoelastic diffusion, and viscoelastic relaxation, and that the magma chamber displays features similar to both end members at different stages during its evolution in time. Based on these features, we identify two characteristic timescales that describe the post-injection evolution of the poroviscoelastic mushy chamber: a short-term post-injection time t_{post}^{short} and a long-term post-injection time t_{post}^{long}. Over t_{post}^{short}, the chamber is dominated by poroelastic diffusion characterized by relatively rapid chamber pressure decrease, crustal tensile increase, and transport (i.e.,leaking) of magma from the fluid region to the mush. t_{post}^{long} indicates the period dominated by viscoelastic relaxation, which is characterized by relatively slow decrease in chamber pressure, increase in tensile stress, and inverse transport (i.e., leaking-back) of magma from the mush region to the fluid region. The two characteristic timescales are determined by material properties and geometry of the chamber, but the short-term timescale is more sensitive to the poroelastic diffusion time $\tau_{diffusion}$, and the long-term timescale to the viscoelastic relaxation time $\tau_{relaxation}$. The features of the post-injection evolution of a poroviscoelastic chamber indicate that the poroelastic diffusion mechanism, which causes higher rates of chamber deformation and strain, is more likely to be relevant for potential interpretation of surface observations, while the viscoelastic relaxation, which causes drastic change in the magma transport direction, is potentially relevant for interpreting petrological and geochemical evidence of crystal growth.

Acknowledgments

We thank James Rice for helpful discussions in the early stages of this work. There is no experimental or observational data associated to this study. Codes for realizing the analytical and semi-analytical solutions are being uploaded to the data repository Vhub, and will be completed upon resubmission.

References

Abate, J., & Whitt, W. (2006). A unified framework for numerically invert-

ing laplace transforms. *INFORMS Journal on Computing*, *18*(4), 408-421. Retrieved from https://doi.org/10.1287/ijoc.1050.0137 doi: 10.1287/ijoc.1050.0137

Bachmann, O., & Huber, C. (2016). Silicic magma reservoirs in the earth's crust. *American Mineralogist*, *101*(11), 2377–2404. Retrieved from http://ammin.geoscienceworld.org/content/101/11/2377 doi: 10.2138/am-2016-5675

Biggs, J., & Pritchard, M. E. (2017). Global volcano monitoring: what does it mean when volcanoes deform? *Elements*, *13*(1), 17-22.

Cashman, K. V., Sparks, R. S. J., & Blundy, J. D. (2017). Vertically extensive and unstable magmatic systems: A unified view of igneous processes. *Science*, *355*(6331). Retrieved from http://science.sciencemag.org/content/355/6331/eaag3055 doi: 10.1126/science.aag3055

Cheadle, M., Elliott, M., & McKenzie, D. (2004). Percolation threshold and permeability of crystallizing igneous rocks: The importance of textural equilibrium. *Geology*, *32*(9), 757-760.

Cheng, A. H.-D. (2016). *Poroelasticity*. Springer International Publishing. doi: doi .org/10.1007/978-3-319-25202-5

Currenti, G., & Williams, C. A. (2014). Numerical modeling of deformation and stress fields around a magma chamber: Constraints on failure conditions and rheology. *Physics of the Earth and Planetary Interiors*, *226*, 14-27.

Dragoni, M., & Magnanensi, C. (1989). Displacement and stress produced by a pressurized, spherical magma chamber, surrounded by a viscoelastic shell. *Physics of the Earth and Planetary Interiors*, *56*(3), 316 - 328. Retrieved from http://www.sciencedirect.com/science/article/pii/0031920189901660 doi: http://dx.doi.org/10.1016/0031-9201(89)90166-0

Ginibre, C., & Wörner, G. (2007). Variable parent magmas and recharge regimes of the parinacota magma system (n. chile) revealed by fe, mg and sr zoning in plagioclase. *Lithos*, *98*(1-4), 118-140.

Ginibre, C., Wörner, G., & Kronz, A. (2002). Minor-and trace-element zoning in plagioclase: implications for magma chamber processes at parinacota volcano, northern chile. *Contributions to Mineralogy and Petrology*, *143*(3), 300-315.

Grosfils, E. B. (2007). Magma reservoir failure on the terrestrial planets: Assessing the importance of gravitational loading in simple elastic models. *Journal of Volcanology and Geothermal Research*, *166*(2).

Gudmundsson, A. (2012). Magma chambers: Formation, local stresses, excess pressures, and compartments. *Journal of Volcanology and Geothermal Research*, *237-238*(Supplement C), 19 - 41. Retrieved from http://www.sciencedirect.com/science/article/pii/S0377027312001539 doi: https://doi.org/10.1016/j.jvolgeores.2012.05.015

Humphreys, M. C., Blundy, J. D., & Sparks, R. S. J. (2006). Magma evolution and open-system processes at shiveluch volcano: Insights from phenocryst zoning. *Journal of Petrology*, *47*(12), 2303-2334.

Huppert, H. E., & Woods, A. W. (2002, 12 05). The role of volatiles in magma chamber dynamics. *Nature*, *420*(6915), 493–495. Retrieved from http://dx.doi.org/10.1038/nature01211

Jellinek, A. M., & DePaolo, D. J. (2003, Jul 01). A model for the origin of large silicic magma chambers: precursors of caldera-forming eruptions. *Bulletin of Volcanology*, *65*(5), 363–381. Retrieved from https://doi.org/10.1007/s00445-003-0277-y doi: 10.1007/s00445-003-0277-y

Karlstrom, L., Dufek, J., & Manga, M. (2010). Magma chamber stability in arc and continental crust. *Journal of Volcanology and Geothermal Research*, *190*(3), 249 - 270. Retrieved from http://www.sciencedirect.com/science/article/pii/S0377027309003977 doi: https://doi.org/10.1016/j.jvolgeores.2009.10.003

Le Mével, H., Feigl, K. L., Córdova, L., DeMets, C., & Lundgren, P. (2015). Evolution of unrest at laguna del maule volcanic field (chile) from insar and gps measurements, 2003 to 2014. *Geophysical Research Letters*, *42*(16), 6590-6598. Retrieved from https://agupubs.onlinelibrary.wiley.com/doi/abs/10.1002/2015GL064665 doi: 10.1002/2015GL064665

Le Mével, H., Gregg, P. M., & Feigl, K. L. (2016, 08). Magma injection into a long-lived reservoir to explain geodetically measured uplift: Application to the 2007–2014 unrest episode at laguna del maule volcanic field, chile. *Journal of Geophysical Research. Solid Earth*, *121*(8), 6092–6108. Retrieved from http://www.ncbi.nlm.nih.gov/pmc/articles/PMC5101856/ doi: 10.1002/2016JB013066

Liao, Y., Soule, S. A., & Jones, M. (2018, 2019/03/11). On the mechanical effects of poroelastic crystal mush in classical magma chamber models. *Journal of Geophysical Research: Solid Earth*, *123*(11), 9376–9406. Retrieved from https://doi.org/10.1029/2018JB015985 doi: 10.1029/2018JB015985

Magee, C., Stevenson, C. T., Ebmeier, S. K., Keir, D., Hammond, J. O., Gottsmann, J. H., ... Petronis, M. S. (2018). Magma plumbing systems: a geophysical perspective. *Journal of Petrology*, *59*(6), 1217-1251.

McKenzie, D. (2011, 05). Compaction and crystallization in magma chambers: Towards a model of the skaergaard intrusion. *Journal of Petrology*, *52*(5), 905–930. Retrieved from http://dx.doi.org/10.1093/petrology/egr009

McTigue, D. F. (1987). Elastic stress and deformation near a finite spherical magma body: Resolution of the point source paradox. *Journal of Geophysical Research: Solid Earth*, *92*(B12), 12931–12940. Retrieved from http://dx.doi.org/10.1029/JB092iB12p12931 doi: 10.1029/JB092iB12p12931

Parmigiani, A., Huber, C., & Bachmann, O. (2014). Mush microphysics and the reactivation of crystal-rich magma reservoirs. *Journal of Geophysical Research: Solid Earth*, *119*(8), 6308-6322.

Perugini, D., Poli, G., & Valentini, L. (2005, Jun 01). Strange attractors in plagioclase oscillatory zoning: petrological implications. *Contributions to Mineralogy and Petrology*, *149*(4), 482–497. Retrieved from https://doi.org/10.1007/s00410-005-0667-6 doi: 10.1007/s00410-005-0667-6

Ruprecht, P., & Wörner, G. (2007). Variable regimes in magma systems documented in plagioclase zoning patterns: El misti stratovolcano and andahua monogenetic cones. *Journal of Volcanology and Geothermal Research*, *165*(3-4), 142-162.

Segall, P. (2016). Repressurization following eruption from a magma chamber with a viscoelastic aureole. *Journal of Geophysical Research: Solid Earth*, *121*(12), 8501–8522. Retrieved from http://dx.doi.org/10.1002/2016JB013597 (2016JB013597) doi: 10.1002/2016JB013597

Segall, P. (2019). Magma chambers: what we can, and cannot, learn from volcano geodesy. *Philosophical Transactions of the Royal Society A: Mathematical, Physical and Engineering Sciences*, *377*(2139), 20180158. Retrieved from https://royalsocietypublishing.org/doi/abs/10.1098/rsta.2018.0158 doi: 10.1098/rsta.2018.0158

Singer, B. S., Le Mével, H., Licciardi, J. M., Córdova, L., Tikoff, B., Garibaldi, N., ... Feigl, K. L. (2018). Geomorphic expression of rapid holocene silicic magma reservoir growth beneath laguna del maule, chile. *Science Advances*, *4*(6). Retrieved from http://advances.sciencemag.org/content/4/6/eaat1513 doi: 10.1126/sciadv.aat1513

Sparks, R. S. J., & Cashman, K. V. (2017). Dynamic magma systems: Implications for forecasting volcanic activity. *Elements*, *13*(1), 35–40. Retrieved from http://elements.geoscienceworld.org/content/13/1/35 doi: 10.2113/gselements.13.1.35

Ward, K. M., Zandt, G., Beck, S. L., Christensen, D. H., & McFarlin, H. (2014).

Seismic imaging of the magmatic underpinnings beneath the altiplano-puna volcanic complex from the joint inversion of surface wave dispersion and receiver functions. *Earth and Planetary Science Letters*, *404*, 43-53.

Zhan, Y., & Gregg, P. (2019). How accurately can we model magma reservoir failure with uncertainties in host rock rheology? *Journal of Geophysical Research: Solid Earth*.

Appendix A Governing equations and solution method

The quantitative treatment of the equations of motions and boundary conditions follows closely (Liao et al., 2018). Specifically, we could obtain the poroviscoelastic solutions by transforming the poroelastic solutions in (Liao et al., 2018) under correspondence principle. The poroviscoelastic rheology can be alternatively expressed using Laplace transform

$$\widetilde{\boldsymbol{\sigma}_m} = (K_m - \frac{2}{3}\overline{\mu_m})\nabla\cdot\widetilde{\vec{u}_m}\boldsymbol{I} + \overline{\mu_m}\left(\nabla\widetilde{\vec{u}_m} + \nabla\widetilde{\vec{u}_m}^T\right) - \alpha\widetilde{P_f}\boldsymbol{I} \tag{A1a}$$

$$\widetilde{m} = \rho_f\alpha(\nabla\cdot\widetilde{\vec{u}_m} + \frac{\alpha}{K_u - K_m}\widetilde{P_f}) \tag{A1b}$$

where the Laplace transform is defined as $\widetilde{f(r,s)} \equiv \int_0^\infty f(r,t)e^{-st}\mathrm{d}t$. The effect of viscous relaxation is reflected by a rigidity that varies with time (i.e., function of s under Laplace transform)

$$\widetilde{\mu_m} = \mu_m\frac{\eta_m s}{\eta_m s + \mu_m}$$

From the equilibrium condition $\nabla\cdot\widetilde{\boldsymbol{\sigma}} = 0 \rightarrow \nabla\left((K_m + \frac{4}{3}\overline{\mu_m})\nabla\cdot\widetilde{\vec{u}} - \alpha\widetilde{P_f}\right) = 0$, we can define time-dependent function $\zeta(t)$ such that its Laplace transform

$$\widetilde{\zeta}(s) = (K_m + \frac{4}{3}\overline{\mu_m})\nabla\cdot\widetilde{\vec{u}} - \alpha\widetilde{P_f}$$

Following steps in (Liao et al., 2018) and non-dimensionelize the system by length scale R_o (chamber radius), time scale η_m/μ_m (relaxation time) and stress/pressure scale μ_r (rock rigidity), the boundary values have the relation

$$\widetilde{P_f}\left(\frac{r_o}{R_o}\right) = \overline{a_1}\widetilde{m}\left(\frac{r_o}{R_o}\right) + \overline{a_2}\widetilde{\zeta} \tag{A2a}$$

$$\widetilde{u_m}\left(\frac{r_o}{R_o}\right) = \overline{b_1}\int_{\frac{r_o}{R_o}}^1 r'^2\widetilde{m}(r')\mathrm{d}r' + \overline{b_2}\widetilde{\zeta} + \widetilde{u_m}(1)\frac{R_o^2}{r_o^2} \tag{A2b}$$

$$\widetilde{\sigma_m^{rr}}\left(\frac{r_o}{R_o}\right) = \overline{c_1}\int_{\frac{r_o}{R_o}}^1 r'^2\widetilde{m}(r')\mathrm{d}r' + \overline{c_2}\widetilde{\zeta} + \overline{c_3}\widetilde{u_m}(1) \tag{A2c}$$

$$\widetilde{\sigma_m^{rr}}(1) = \widetilde{\zeta} - 4\frac{\overline{\mu_m}}{\mu_r}\widetilde{u_m}(1) \tag{A2d}$$

$$\widetilde{P_l} = \overline{d_1}\int_{\frac{r_o}{R_o}}^1 r^2\widetilde{m}(r)\mathrm{d}r + \overline{d_2}\widetilde{\zeta} - \frac{3K_lR_o^3}{\mu_r r_o^3}\widetilde{u_m}(1) + \overline{f_4} \tag{A2e}$$

where $\overline{f_4} = \frac{K_l}{\mu_r}\frac{\Delta M}{M_o}\frac{1}{s}$ (for instantaneous injection) or $\overline{f_4} = \frac{K_l}{\mu_r}\frac{\Delta M}{M_o}\frac{1-e^{st_{inj}}}{s^2t_{inj}}$ (for gradual injection), and the s-dependent coefficients $\overline{a_1}, \overline{a_2}, \overline{b_1}, \overline{b_2}, \overline{c_1}, \overline{c_2}, \overline{d_1}, \overline{d_2}$ have the same forms as those defined in Appendix A.2.4 in (Liao et al., 2018) while substituting $\overline{\mu}(s)$ for mush rigidity. Substituting (A2) into the boundary conditions and into Darcy's law, mass conservation, and equilibrium condition, we obtain (dimensionless) constraint on the fluid content $\widetilde{m}$

$$\nabla^2\widetilde{m} - \frac{\tau_{diffusion}}{\tau_{relaxation}}\frac{s(s + \frac{K_u}{K_u + \frac{4}{3}\mu_m^o})}{(s + \frac{K_m}{K_m + \frac{4}{3}\mu_m^o})}\widetilde{m} = 0 \tag{A3}$$

and the boundary conditions

$$\frac{\partial \widetilde{m}}{\partial r}(r=1)=0, \qquad \widetilde{a_1}\widetilde{m}(\frac{r_o}{R_o})+\overline{h_o}\int \widetilde{m}r^2dr=\overline{h1}$$

where $\overline{h_0}$ and $\overline{h_1}$ have the same form of h_0 and h_1 in §A.2.4 in (Liao et al., 2018) with $\mu_m \to \overline{\mu_m}$. Solving (A3) with the boundary conditions and using the relations between m, $\vec{u}$ and P_f similar to those in (Liao et al., 2018), we can find the solutions for $\widetilde{m}$

$$\widetilde{m}=\frac{Ae^{r\sqrt{S_o}}}{\sqrt{S_o}r}+\frac{Be^{-r\sqrt{S_o}}}{\sqrt{S_o}r} \tag{A4}$$

with

$$S_o=\frac{\tau_{diffusion}}{\tau_{relaxation}}\frac{s(s+\frac{K_u}{K_u+\frac{4}{3}\mu_m^o})}{(s+\frac{K_m}{K_m+\frac{4}{3}\mu_m^o})}, \qquad A=\frac{\widetilde{h_1}S_o^{\frac{3}{2}}(\sqrt{S_o}+1)e^{-\sqrt{S_o}}}{2\overline{g}}, \qquad B=\frac{\widetilde{h_1}S_o^{\frac{3}{2}}(\sqrt{S_o}-1)e^{\sqrt{S_o}}}{2\overline{g}}$$

$$\overline{g}=\sqrt{S_o}\left(\frac{\overline{a_1}R_o}{r_o}S_o+\overline{h_0}\left(1-\frac{r_o}{R_o}\right)\right)\cosh\left(\sqrt{S_o}\left(1-\frac{r_o}{R_o}\right)\right)+\left(\left(\overline{h_0}\frac{r_o}{R_o}-\frac{\overline{a_1}R_o}{r_o}\right)S_o-\overline{h_0}\right)\sinh\left(\sqrt{S_o}\left(1-\frac{r_o}{R_o}\right)\right)$$

The Laplace transform of other quantities can all be obtained via (A4), such as core pressure, rock tensile stress and radial stress at the chamber's wall

$$\begin{aligned}
&\widetilde{\sigma^{\theta\theta}_{rock}}(1)=-2\frac{\overline{f_4}}{\overline{g_2}}-2\frac{\overline{g_1}}{\overline{g_2}}\int_{\frac{r_o}{R_o}}^{1}\widetilde{m}r^2dr\\
&\widetilde{\sigma^{rr}_{m}}(1)=\widetilde{\sigma^{rr}_{rock}}(1)=-2\widetilde{\sigma^{\theta\theta}_{rock}}(1)\\
&\widetilde{\zeta}=2\left(4\frac{\overline{\mu_m}}{\mu_r}-1\right)\widetilde{\sigma^{\theta\theta}}\\
&\widetilde{P_l}=\overline{a_1}\widetilde{m}\left(\frac{r_o}{R_o}\right)+\overline{a_2}\widetilde{\zeta}
\end{aligned} \tag{A5}$$

Following (McTigue, 1987), we apply a first order correction to obtain surface deformation. The pressure-stress coupling in (McTigue, 1987) is here replaced by a stress-stress coupling at the chamber-crust interface, and the radial component of poroviscoelastic stress plays the role of a virtual pressure in the chamber, leading to the surface deformation (McTigue, 1987; Segall, 2016)

$$\begin{aligned}
\widetilde{u_z}(\rho,0)&=-\widetilde{\sigma^{rr}_{m}}(1)\frac{d}{R_0}\left(\frac{R_0}{d}\right)^3\frac{1-\nu}{\left(\frac{\rho^2}{d^2}+1\right)^{\frac{3}{2}}}\\
\widetilde{u_\rho}(\rho,0)&=-\widetilde{\sigma^{rr}_{m}}(1)\frac{\rho}{R_0}\left(\frac{R_0}{d}\right)^3\frac{1-\nu}{\left(\frac{\rho^2}{d^2}+1\right)^{\frac{3}{2}}}
\end{aligned} \tag{A6}$$

where u_z and u_ρ are vertical and horizontal displacement on the surface (normalized by chamber radius R_0) measured at distance ρ from the center of the chamber's projection, ν is Poisson's ratio of the elastic crust. We numerically invert the Laplace solutions to obtain solutions using a matlab code shared on Mathworks File Exchange, which is based on the scheme proposed in (Abate & Whitt, 2006). The Laplace solution allows us to define the longest timescale in the system. Similar to (Liao et al., 2018), the Laplace solutions can be inverted using the Mellin inversion formula, which yields the solutions in real space as a superposition of exponentially decaying terms in the form of

$$A(r,t)=A_0(r)+A_1(r)e^{-t/\tau_1}+A_2(r)e^{-t/\tau_2}+...$$

where τ_1 is the largest decay period, and can be solved graphically given the parameters of the system. We use this timescale to determine the longest timescale in the system's post-injection evolution t_{post}^{long} (Liao et al., 2018).

Appendix B Additional model results

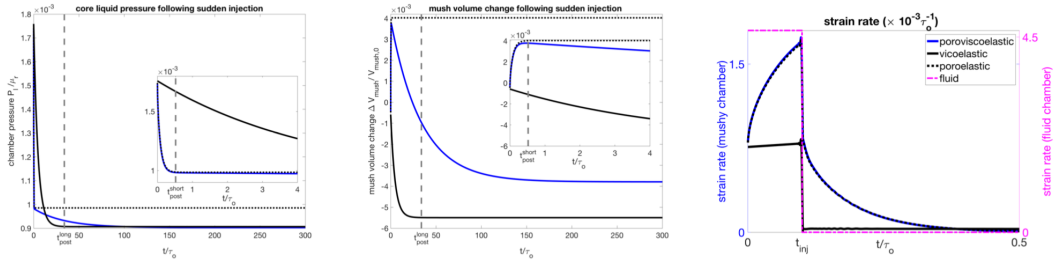

(a) (b) (c)

[H]

Figure B1. Panel (a) and (b): post-injection short-term and long-term evolution for core pressure and mushy deformation for three cases (poroviscoelastic, poroelastic, and viscoelastic). Inset panels are zoom-in of the beginning period of the evolution, and grey broken lines indicate the two post-injection timescales t_{post}^{long} and t_{post}^{short}. Panel (c): tensile strain rate $\dot{\epsilon}^{\theta\theta} = \dot{u}(R_o)/R_o$ at the wall of the chamber during and after the injection, for four different cases. For mushy chamber, the strain rate is highest at the end of the injection, and remains positive during short-term post-injection evolution. During long-term post-injection evolution, the strain rate becomes indiscernible.

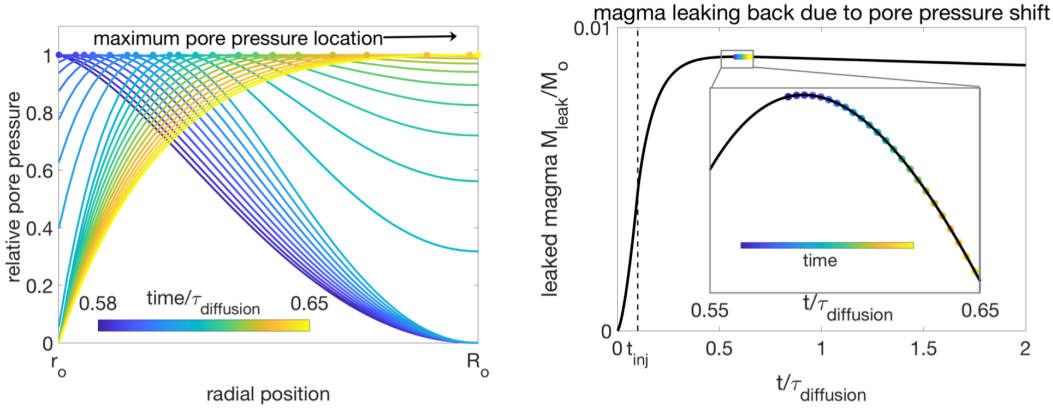

(a) (b)

[H]

Figure B2. Panel (a) cumulative amount of leaked magma M_{leak} as a function of time during and after the injection. Panel (b) shows the the relative pore pressure $\frac{P_f - min(P_f)}{max(P_f) - min(P_f)}$ as function of radial position in the mush shell. Colored lines in (b) correspond to colored data points in (a). The decrease in M_{leak} with time corresponds to the shift of maximum pore pressure from the inner boundary of the much outwards.

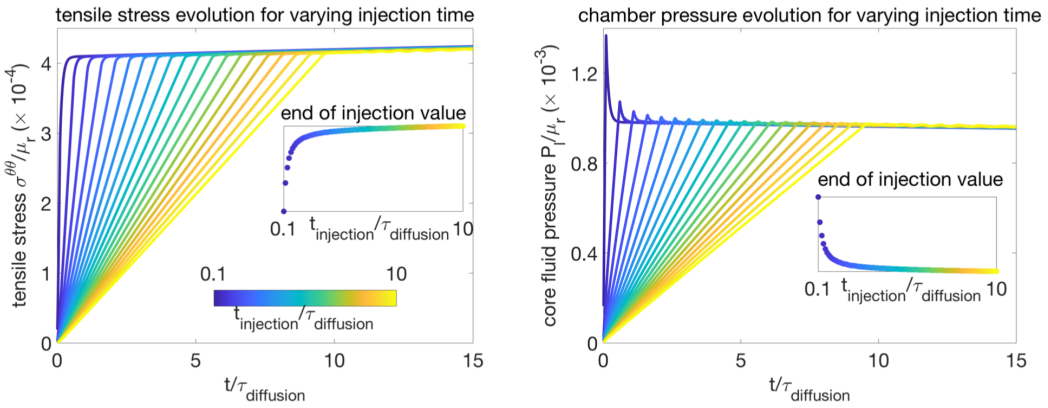

[H]

Figure B3. Evolution of core pressure and tensile stress with time for varying injection time length t_{inj}. The system has $\tau_{diffusion} = \tau_{relaxation}$. Insets show the values at the end of the injection. As t_{inj} increases, the short-term evolution period shortens and become less apparent.